



## Phase vortex lattices in neutron interferometry

Niels Geerits <sup>1✉</sup>, Hartmut Lemmel <sup>1,2</sup>, Anna-Sophie Berger<sup>1</sup> & Stephan Sponar <sup>1✉</sup>

Neutron Orbital Angular Momentum (OAM) is an additional quantum mechanical degree of freedom, useful in quantum information, and may provide more complete information on the neutron scattering amplitude of nuclei. Various methods for producing OAM in neutrons have been discussed. In this work we generalize magnetic methods which employ coherent averaging and apply this to neutron interferometry. Two aluminium prisms are inserted into a nested loop interferometer to generate a phase vortex lattice with significant extrinsic OAM,  $\langle L_z \rangle \approx 0.35$ , on a length scale of  $\approx 220 \mu\text{m}$ , transverse to the propagation direction. Our generalized method exploits the strong nuclear interaction, enabling a tighter lattice. Combined with recent advances in neutron compound optics and split crystal interferometry our method may be applied to generate intrinsic neutron OAM states. Finally, we assert that, in its current state, our setup is directly applicable to anisotropic ultra small angle neutron scattering.

<sup>1</sup>Atominstitut, Technische Universität Wien, Stadionallee 2, 1020 Vienna, Austria. <sup>2</sup>Institut Laue-Langevin, 71 Avenue des Martyrs, CS 20156, 38042 Grenoble Cedex 9, France. ✉email: [niels.geerits@tuwien.ac.at](mailto:niels.geerits@tuwien.ac.at); [stephan.sponar@tuwien.ac.at](mailto:stephan.sponar@tuwien.ac.at)

First observed in optics<sup>1–3</sup>, Orbital Angular Momentum (OAM) of photons has become ubiquitous in physics. Seeing applications in quantum communications<sup>4</sup>, astronomy<sup>5</sup>, and many other areas<sup>6</sup>, OAM has also been observed in massive free particles, such as electrons<sup>7,8</sup>, atoms<sup>9</sup>, and neutrons<sup>10,11</sup>.

It is expected that neutron OAM will open up new avenues in scattering, allowing one to directly access the complex phase of the scattering amplitude<sup>12,13</sup>. In addition, neutron OAM marks an additional degree of freedom, applicable to quantum information and contextuality<sup>14,15</sup>. Coupling OAM to the other degrees of freedom in a neutron has been discussed in other papers<sup>16,17</sup>. While not a topic of this paper, in combination with the path, spin and energy of the neutron, the additional degree of freedom, provided by OAM, would enable the first quadruply entangled matter wave beam to our knowledge. Quantum mechanical OAM is a type of azimuthal phase structure on the wavefunction of the form  $e^{i\ell\phi}$ , with  $\phi$  the azimuthal coordinate. Due to continuity conditions  $\ell$  can only take on integer values. Therefore OAM, unlike spin angular momentum, is not an intrinsic property of the neutron, but a property arising from the spatial structure of the wavefunction. Hence, OAM states are some times also referred to as spatial helicity states<sup>18</sup>.

The first experiment claiming neutron OAM<sup>10</sup>, is controversial due to ambiguity on whether any of the observed OAM is intrinsic to the neutrons or whether it is simply an extrinsic beam property<sup>19</sup>, since the dimensions of the phase vortex, henceforth referred to as the vortex diameter, observed from the spiral phase plate<sup>10</sup> were much larger than the neutron transverse coherence length (order 100 nm). Furthermore, if the neutrons possessed intrinsic OAM the beam could likely only be represented by a mixed state. To address these concerns a method using magnetic prisms was developed to generate a lattice of vortices, with smaller vortex diameters<sup>20</sup>. In addition, the use of static electric fields has been explored<sup>21</sup>. However, realistically achievable electric and magnetic potentials are too small to generate vortex diameters on the order of the neutron transverse coherence length. Recently a large lattice of microscopic fork gratings was produced with the goal of producing intrinsic OAM states in a collimated cold neutron beam<sup>11</sup>. It is likely that significant intrinsic OAM was produced. Though important challenges remain such as the production of significant intrinsic OAM in thermal neutron beams or a definitive method of distinguishing intrinsic and extrinsic OAM.

In this paper, we address the challenge of generating OAM in thermal neutrons by generalizing the magnetic coherent averaging method<sup>20</sup>, such that the strong nuclear potential can be exploited, enabling production of smaller vortex diameters at thermal energies. We demonstrate the generation of a vortex lattice using strongly interacting aluminium prisms in a nested loop neutron interferometer. Previously prisms have been employed in neutron interferometry for holography<sup>22</sup>. In an interferometer, a single input wavefunction can be split into multiple partial wavefunctions each of which can undergo a simple and independent transformation in each path of the interferometer. When the modified partial wavefunctions of each path are recombined more complicated structures may arise. In a two path, single loop, interferometer the combination of a phase shifter and a pair orthogonal prisms enables us to generate a composite wavefunction exhibiting azimuthal structure where the  $\ell = \pm 1$  mode amplitude is significant. To extract the phase structure of the composite wavefunction an additional reference beam is needed. For this purpose, a three path nested loop interferometer was used.

## Results

**Experimental setup.** The experiment was carried out at a wavelength of 1.92 Å on the thermal neutron interferometry

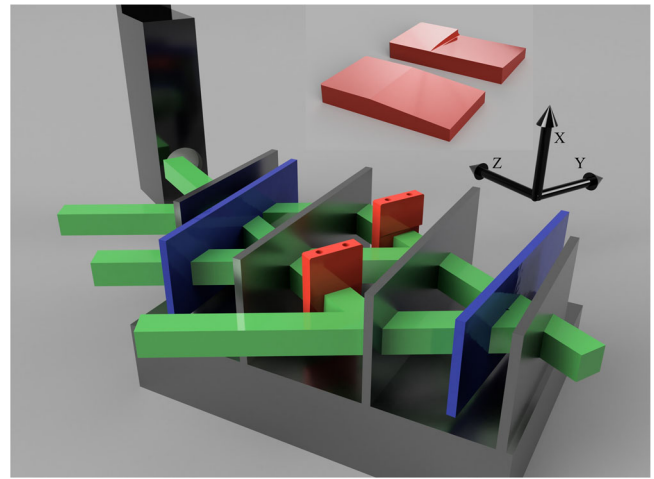


**Fig. 1 Setup schematic.** Sketch of the 4 plate interferometer (145 mm long), containing two (red) orthogonal prisms (blown up on the top portion) and two phase shifters (blue). The neutron beam, coming from the right, forms three loops, two small ones between the first and third and second and fourth plate respectively and a large loop between the first and last plate. The phase shifters can be rotated around the vertical to induce phase shifts between the paths in their respective loops. A position sensitive detector is shown in black. Additionally, in black the coordinate convention used in this paper is shown.

station, S18, at the high-flux reactor of the Institute Laue Langevin (ILL) in Grenoble, France<sup>23</sup>. Our setup is shown in Fig. 1. This interferometer generates three nested loops<sup>24–27</sup>, two small loops between the first and third plate and the second and fourth plate, respectively, and a large loop between the first and fourth plate. Our prisms each have a 5 degree slope and are made from aluminium. To control the phase difference of each loop a minimum of two phase shifters are required. These phase shifters consist of flat silicon and sapphire slabs.

**Theoretical model.** In the case of thermal neutrons where the nuclear potential is low compared to the kinetic energy, the action of a prism can be approximated by a translation of the reciprocal wavefunction (i.e., by convolving with a delta function)  $\psi'(\mathbf{k}) = \psi_0(\mathbf{k}) * \delta(\mathbf{k} - \mathbf{k}')$ , while phase shifters imprint a global phase on the wavefunction  $\psi'(\mathbf{k}) = e^{i\alpha}\psi_0(\mathbf{k})$ . In principle prisms also apply a global phase to the wavefunction, however, in this paper, we choose to account for this phase in the action of the phase shifter. The input wavefunction (in k-space) is assumed to be Gaussian

$$\psi_0(\mathbf{k}) = \sqrt{\frac{1}{2\pi\zeta^2}} e^{-\frac{(k_x^2 + k_y^2)}{4\zeta^2}} \Phi(k_z) \quad (1)$$

with  $k_x$  and  $k_y$  denoting the transverse wavenumbers and  $\zeta$  the transverse momentum spread, related to the average divergence of individual neutrons,  $\theta$ , by  $\zeta \approx k_z\theta$ , for small  $\theta$ .  $\Phi(k_z)$  refers to the longitudinal part of the reciprocal wavefunction that is virtually unaffected by the action of the prisms. The composite wavefunction projected from the last interferometer plate to the detector can then be written as

$$\psi_1(\mathbf{k}) = \frac{1}{\sqrt{3}} [\psi_0(\mathbf{k}) + e^{i\alpha_1}\psi_0(\mathbf{k} - k_{\perp}\hat{y}) + e^{i\alpha_2}\psi_0(\mathbf{k} - k_{\perp}\hat{x})] \quad (2)$$

where the transverse momentum shift,  $k_{\perp}$ , is related to the angle of refraction,  $\gamma$ , induced by the prisms  $k_{\perp} = k_z\gamma$ . It is instructive to look at Eq. (2) in real space cylindrical coordinates,  $(\rho, \phi, z)$ , since the real space equation allows us to more easily deduce the

angular momentum properties of this wavefunction.

$$\psi_1(\mathbf{r}) = \frac{1}{\sqrt{3}}\psi_0(\mathbf{r})[1 + e^{i\alpha_1} e^{ik_{\perp}\rho \sin(\phi)} + e^{i\alpha_2} e^{ik_{\perp}\rho \cos(\phi)}] \quad (3)$$

The expression  $\psi_0(\mathbf{r}) = \sqrt{\frac{2}{\pi\sigma^2}} e^{-\frac{\rho^2}{\sigma^2}} \Phi(z)$  is the Fourier transform of (1).  $\sigma = \frac{1}{\zeta}$  denotes the real space coherence length and  $\Phi(z)$  is the real space component of the wavefunction along the  $z$  direction. We require that  $\Phi(z)$  is normalized (i.e.,  $\int dz |\Phi(z)|^2 = 1$ ). From here on out it is important to distinguish between the constant reference wavefunction,  $\psi_0(\mathbf{r})$ , and the test wavefunction  $\psi_t(\mathbf{r})$ , which is postulated to carry OAM.

$$\begin{aligned} \psi_t(\mathbf{r}) &= \frac{1}{\sqrt{2}}\psi_0(\mathbf{r})(e^{ik_{\perp}\rho \sin(\phi)} + e^{i\Delta\alpha} e^{ik_{\perp}\rho \cos(\phi)}) \\ \psi_1(\mathbf{r}) &= \frac{1}{\sqrt{3}}[\psi_0(\mathbf{r}) + \sqrt{2}e^{i\alpha_1}\psi_t(\mathbf{r})] \end{aligned} \quad (4)$$

with  $\Delta\alpha = \alpha_2 - \alpha_1$ . We note that the above wavefunctions are not properly normalized, since they do not represent the total neutron wavefunction emerging from the interferometer, but only the part of the wavefunction projected towards the detector.

**Treatment of OAM.** To calculate the total OAM of a wavefunction around the  $z$ -axis (propagation direction), we introduce the OAM operator

$$L_z = -i \left[ x \frac{\partial}{\partial y} - y \frac{\partial}{\partial x} \right] = -i \frac{\partial}{\partial \phi} \quad (5)$$

and its expectation value

$$\langle L_z \rangle = -i \frac{\int d\mathbf{r} \psi^*(\mathbf{r}) \frac{\partial}{\partial \phi} \psi(\mathbf{r})}{\int d\mathbf{r} |\psi(\mathbf{r})|^2} \quad (6)$$

Applying this calculation to the test wave function described in Eq. (4), we can determine the expected average OAM for various combinations of transverse coherence lengths and refraction angles. It can be shown (see Supplementary Note 1) that integrating Eq. (6) over  $\phi$  for  $\psi_t(\mathbf{r})$  leads to the following expression for the total OAM

$$\langle L_z \rangle = \sqrt{2}\pi \sin(\Delta\alpha) \frac{\int d\rho k_{\perp} \rho^2 |\psi_0|^2 J_1(\sqrt{2}k_{\perp}\rho)}{\int d\mathbf{r} |\psi(\mathbf{r})|^2} \quad (7)$$

In the case of our Gaussian  $\psi_0(\mathbf{r})$  this is a standard Hankel transform with the result

$$\langle L_z \rangle = \sin(\Delta\alpha) \frac{k_{\perp}^2 \sigma^2}{4N} e^{-\frac{k_{\perp}^2 \sigma^2}{4}} \quad (8)$$

with the normalization parameter  $N = \int d\mathbf{r} |\psi(\mathbf{r})|^2 = 1 + \cos(\Delta\alpha) e^{-\frac{k_{\perp}^2 \sigma^2}{4}}$ . For large  $k_{\perp}$ , the normalization parameter goes to unity. We can easily see in this limit that the OAM is maximal/minimal for  $\Delta\alpha = \pm \pi/2$ . In addition using  $N \approx 1$  and the derivative of Eq. (8) we find the approximate value of  $k_{\perp}$  for which the OAM is maximized/minimized:  $k_{\perp} = \pm \frac{2}{\sigma} = \pm 2\zeta$ . That is to say that the refraction angle must be about the order of magnitude of the average momentum spread of an individual neutron for maximal OAM. Another interesting region of Eq. (8), is found for small  $k_{\perp}$  in the vicinity of  $\Delta\alpha \approx \pi$ . Here, around  $\Delta\alpha = \pi$ , the OAM may vary rapidly and even attain a significant value for a relatively small value of  $k_{\perp}$ .

The form of Eq. (5) seems to imply that the total OAM depends on the choice of the location of the  $z$ -axis in the  $x$ - $y$  plane. However, for some wavefunctions  $\langle L_z \rangle$  is translation invariant. In these cases, the OAM is intrinsic<sup>28,29</sup>. For particles, it can be shown that under a translation (with  $x' = x - x_0$  and

$y' = y - y_0$ ) the OAM changes by

$$\langle \Delta L_z \rangle = -i \int d\mathbf{r} \psi^*(\mathbf{r}) \left[ x_0 \frac{\partial}{\partial y} - y_0 \frac{\partial}{\partial x} \right] \psi(\mathbf{r}) \quad (9)$$

Thus it follows that OAM is intrinsic if the expectation values of both transverse momentum components are zero.

$$\langle k_x \rangle = \langle k_y \rangle = 0 \quad (10)$$

Since for our setup  $\langle k_x \rangle = \langle k_y \rangle = k_{\perp}$  and  $k_{\perp}\sigma$  is at most 0.01, we can consider the OAM to be quasi intrinsic, since  $k_{\perp}r_0 \approx 0$ . As the interaction range of the neutron is proportional to its' coherence length it does not make sense to look at  $r_0 \gg \sigma$  when examining the OAM of single neutrons. In addition to the expectation value it is instructive to look at the OAM spread, defined as a standard deviation:

$$\chi = \sqrt{\langle L_z^2 \rangle - \langle L_z \rangle^2} \quad (11)$$

with the second moment given by (see Supplementary Note 1 for a complete derivation)

$$\langle L_z^2 \rangle = \frac{k_{\perp}^2 \sigma^2}{4N} - \cos(\Delta\alpha) \frac{k_{\perp}^4 \sigma^4}{16N} e^{-\frac{\sigma^2 k_{\perp}^2}{4}} \quad (12)$$

It can be seen that the OAM bandwidth is maximal for a phase shift  $\Delta\alpha = \pm \pi$ . Both the OAM bandwidth and the expectation value are shown for a variety of  $\Delta\alpha$  and  $k_{\perp}$  (in units of  $\zeta$ ) in Fig. 2. At this point it should be pointed out that in the case of perfect crystal neutron interferometry, the momentum spread  $\zeta$  is direction dependent, such that the input wavefunction should be written as

$$\psi_0(\mathbf{k}) = \sqrt{\frac{1}{2\pi\zeta_x\zeta_y}} e^{-\frac{(\zeta_x^2 k_x^2 + \zeta_y^2 k_y^2)}{4\zeta_x^2\zeta_y^2}} \Phi(k_z) \quad (13)$$

where  $\zeta_x$  and  $\zeta_y$  differ by three orders of magnitude. Nonetheless, the above theory for isotropic momentum spread ( $\zeta_x = \zeta_y = \zeta$ ) is still valid if the transverse momentum shifts induced by the prisms are adapted to the momentum spread in the respective direction. However, the experiment described in this paper employed identical prisms, hence it is possible that Fig. 2 does not give an accurate representation of the quasi-intrinsic OAM of our wavefunction. Nonetheless, when we calculate Eq. (6) analytically (the step-by-step calculation is shown in Supplementary Note 1), using the  $\psi_0(\mathbf{r})$  implied by Eq. (13), it can be shown that

$$\langle L_z \rangle = \sin(\Delta\alpha) \frac{k_{\perp}^2 (\sigma_x^2 + \sigma_y^2)}{8N} e^{-\frac{k_{\perp}^2 (\sigma_x^2 + \sigma_y^2)}{8}} \quad (14)$$

which in form is identical to Eq. (8). This expression becomes completely identical to Eq. (8), if we define an effective transverse coherence  $\sigma^2 = (\sigma_x^2 + \sigma_y^2)/2$ , the normalization parameter  $N$  is then unchanged. So Fig. 2 can also be considered for anisotropic momentum spreads and the maximal amount of OAM generated by this type of setup is not affected by an anisotropic momentum distribution. It follows that in the experiment described here the effective  $k_{\perp}\sigma$  is on the order of 0.015

Given this effective  $k_{\perp}\sigma$ , we may regard the OAM as quasi intrinsic. However, as can be seen in Fig. 2, the OAM production is small for this configuration. Nonetheless, it is instructive to look at the amplitudes of the wavefunctions first OAM modes for small  $k_{\perp}\sigma$ . To this end, we introduce the azimuthal Fourier transform (AFT)

$$\psi^{\ell}(\rho, z) = \frac{1}{\sqrt{2\pi}} \int_0^{2\pi} \psi(\mathbf{r}) e^{i\ell\phi} d\phi \quad (15)$$

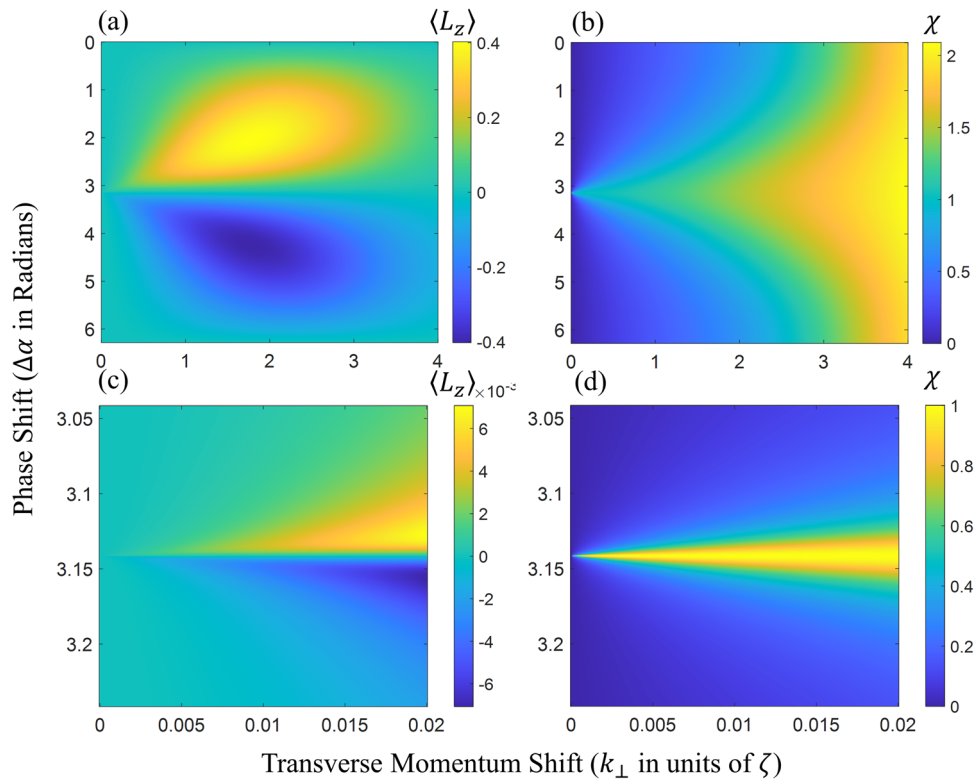


**Fig. 2 OAM expectation value and bandwidth.** **a** Expectation value of the OAM for the test wavefunction (Eq. (4)) as given by the analytical expression in Eq. (8) for various transverse momentum shifts  $k_\perp$  and phase shifts  $\Delta\alpha$ . Around  $\Delta\alpha = \pm\pi/2$  and  $k_\perp = 4\pi$  the OAM attains a maximal/minimal value of  $\pm 0.4$  **b** The OAM bandwidth defined by Eq. (11) for  $\psi_t$  as a function of transverse momentum shift  $k_\perp$  and phase shift  $\Delta\alpha$ . Inserts **(c)** and **(d)** show the behavior of  $\langle L_z \rangle$  and  $\chi$ , respectively, for small  $k_\perp$  in the vicinity of  $\Delta\alpha = \pi$ . In all figures  $k_\perp$  is in units of  $\zeta$ . In the case of the described experiment the normalized  $k_\perp$  ranges from  $10^{-5}$  (vertical refraction) to 0.02 (horizontal refraction).

and its inverse

$$\psi(\mathbf{r}) = \frac{1}{\sqrt{2\pi}} \sum_\ell \psi^\ell(\rho, z) e^{-i\ell\phi} \tag{16}$$

where the probability amplitude of the  $\ell$ th OAM mode is given by

$$A^\ell = \frac{\int d\rho dz \rho |\psi^\ell(\rho, z)|^2}{\sum_\ell \int d\rho dz \rho |\psi^\ell(\rho, z)|^2} \tag{17}$$

Hence by applying the AFT to a wavefunction, we can determine the amplitude of each OAM mode individually. The AFT of the test wavefunction (Eq. (4)) is given by the Jacobi-Anger expansion<sup>30</sup>

$$\psi_t^\ell(\rho) = (-1)^\ell \frac{2}{\sigma} e^{-\frac{\rho^2}{\sigma^2}} J_\ell(k_\perp \rho) (1 + i^{-\ell} e^{i\Delta\alpha}) \tag{18}$$

Note that we have dropped the longitudinal part of the wavefunction,  $\Phi(z)$  for this analysis. Realistically the refraction angle induced by a neutron optical prism is much smaller than the beam divergence. Therefore, the width of the Gaussian envelope in Eq. (18) is much smaller than the period of the Bessel functions,  $J_\ell(k_\perp \rho)$ . This implies that linearizing the Bessel functions will yield a good approximation of the OAM amplitudes. We note that in the linear limit only Bessel functions of modes  $\ell = -1, \ell = 0$  and  $\ell = 1$  are non zero, therefore, only these OAM modes play a non-vanishing role in our wavefunction. The approximation yields

$$\begin{aligned} \psi_t^{\ell=0}(\rho) &\approx \frac{2}{\sigma} e^{-\frac{\rho^2}{\sigma^2}} (1 + e^{i\Delta\alpha}) \\ \psi_t^{\ell=\pm 1}(\rho) &\approx \mp \frac{k_\perp \rho}{\sigma} e^{-\frac{\rho^2}{\sigma^2}} (1 \mp i e^{i\Delta\alpha}) \end{aligned} \tag{19}$$

As previously shown, the average OAM  $\langle L_z \rangle$  is zero for  $\Delta\alpha = \pm\pi$ .

However, this new analysis shows that, despite this, the intrinsic neutron OAM is dominated by an equal superposition of  $\ell = \pm 1$  modes, while the  $\ell = 0$  mode is totally suppressed. We may calculate the probability amplitudes of the  $\ell = 0$  and  $\ell \pm 1$  modes, according to Eq. (17), using our approximate expressions in Eq. (19). Figure 3 shows these probability amplitudes for various  $k_\perp$  around  $\Delta\alpha = \pi$ . It can be seen that for increasing  $k_\perp$  the  $\ell = 1$  and  $\ell = -1$  probabilities widen and begin to separate from one another. It can also be seen that the  $\ell = 1$  and  $\ell = -1$  amplitudes are asymmetric around  $\Delta\alpha = \pi$ , having a steeper slope to one side of the peak compared to the other side. This results in the OAM becoming net positive for  $\Delta\alpha < \pi$  and negative for phase shifts above  $\pi$ .

**Macroscopic treatment.** Until now, we have considered a microscopic treatment where a single wavefunction is centered on the optical axis. Now we turn to the macroscopic treatment where we consider an ensemble of quasi-paraxial wavefunctions which make up a beam. This is also the scale at which vortex lattices can appear, which carry macroscopic beam OAM. Since the individual neutrons that make up the beam can be far off-axis, compared to their coherence length, Eq. (9) predicts that most neutrons will have extrinsic OAM with respect to the axis around which (beam) OAM is defined. In our and most other neutron experiments with OAM the main qualitative difference between extrinsic and intrinsic OAM, that can be observed, is the vortex diameter as can be grasped by looking at Eq. (9). As the vortex diameter grows the more variability is introduced to the observed OAM of an individual neutron some distance from the vortex center (assuming  $\langle k_x \rangle \neq 0$  and/or  $\langle k_y \rangle \neq 0$ ). As a rough definition we may say in the case of (quasi) intrinsic OAM the vortex



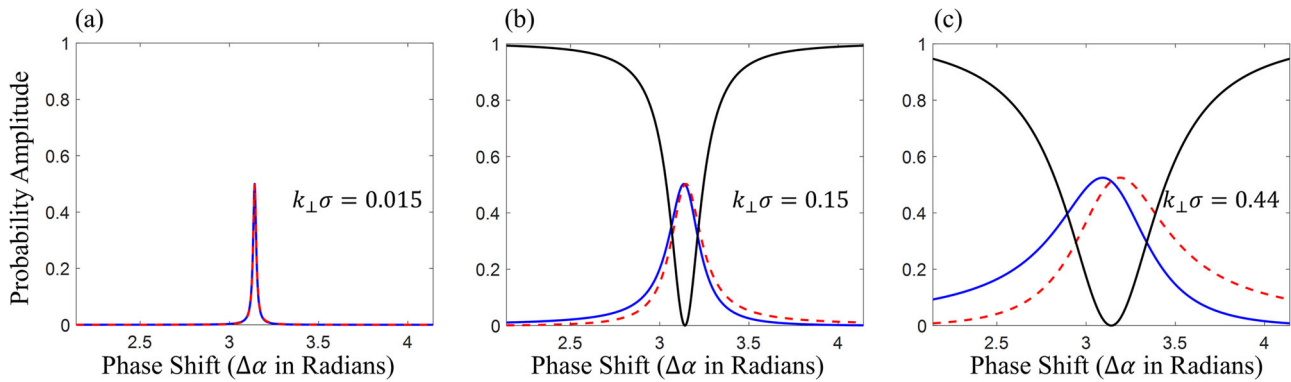


**Fig. 3 Probability amplitudes of the first and zeroth order OAM modes.** The first order mode probabilities  $\ell = 1$  (blue),  $\ell = -1$  (red dashed) and the zeroth order mode probability  $\ell = 0$  (black) are plotted against the phase shift  $\Delta\alpha$  (centered on  $\Delta\alpha = \pi$ ) for various transverse momentum shifts, (a) equal to the experimental case  $k_{\perp}\sigma = 0.015$ , (b) ten times larger and (c) thirty times larger than in the experimental case. In (a) the  $\ell = 0$  amplitude is not plotted for improved visibility. It can be clearly discerned that  $\ell = \pm 1$  probabilities widen for increasing refraction,  $k_{\perp}$ . In addition, the  $\ell = 1$  and  $\ell = -1$  probabilities appear to be mirror images of one another (mirrored around  $\Delta\alpha = \pi$ ).

should manifest on a length scale comparable to the transverse coherence length, while in the case of extrinsic OAM the vortex may exceed this length by many orders of magnitude. It has been predicted that neutrons carrying intrinsic OAM may interact differently with matter, such as in scattering from microscopic targets<sup>12,13</sup> or polarized nuclear targets<sup>31</sup>. Hence some neutron scattering and transmission measurements may be able to distinguish between intrinsic and extrinsic OAM.

It is well known that a prism inserted into a single loop interferometer generates a Moire fringe pattern along the refraction direction<sup>32</sup>. In our nested loop interferometer, the Moire patterns generated by each loop are overlaid, thereby creating a lattice like structure. The spatial intensity profile can be calculated using the wavefunction projected to the detector (Eq. (3)). The wave function impinging on the detector at position  $\mathbf{r}'$  is simply Eq. (3) with the input wavefunction  $\psi_0(\mathbf{r})$  translated by  $\mathbf{r}'$

$$\psi_1(\mathbf{r} - \mathbf{r}') = \frac{1}{\sqrt{3}} \psi_0(\mathbf{r} - \mathbf{r}') [1 + e^{i\alpha_1} e^{ik_{\perp}y} + e^{i\alpha_2} e^{ik_{\perp}x}] \quad (20)$$

The intensity profile which is measured can be calculated by taking the absolute value squared of Eq. (20):

$$I(\mathbf{r}') = \int_{\mathcal{P}} d\mathbf{r} |\psi_1(\mathbf{r} - \mathbf{r}')|^2 \quad (21)$$

with  $\mathcal{P}$  a domain given by the pixel size of the detector, which is quasi infinite in size compared to the wavefunction. Assuming  $\mathbf{r}'$  falls within the domain  $\mathcal{P}$ , we may approximate this integral by

$$I(\mathbf{r}') = \frac{1}{3} \int_{\mathcal{P}} d\mathbf{r} \delta(\mathbf{r} - \mathbf{r}') [3 + 2 \cos(k_{\perp}y + \alpha_1) + 2 \cos(k_{\perp}x + \alpha_2) + 2 \cos(k_{\perp}(x - y) + \Delta\alpha)] \quad (22)$$

where we used that  $|\psi_0(\mathbf{r} - \mathbf{r}')|^2$  may be approximated by a delta function since the coherence length is very small compared to the period of the cosines. Hence it follows

$$I(\mathbf{r}') = \frac{1}{3} [3 + 2 \cos(k_{\perp}y + \alpha_1) + 2 \cos(k_{\perp}x + \alpha_2) + 2 \cos(k_{\perp}(x - y) + \Delta\alpha)] \quad (23)$$

For the prisms used in this experiment, we expect a value of  $k_{\perp}$  which corresponds to a lattice period of 1.75 mm.

**Measurements.** The vortex lattice generated by our setup is shown in Fig. 4a. In addition, the figure contains a fit (Fig. 4b) based on Eq. (23). The discrepancies between the fit and the data could be explained by different amplitudes of the three Cosine

terms in Eq. (23). These amplitudes can differ depending on the amount of material each partial wavefunction in the interferometer goes through. If two paths “see” a similar amount of material, the amplitude of the Moire fringes from that loop will be large, while if there is a discrepancy in the amount of material, dephasing may occur, thereby lowering the amplitude of the respective loop.

Since the model used for our fit assumes that the intensity is given by  $|\psi_1(\mathbf{r})|^2$ , we may extract a part of the test wavefunction,  $\psi_1(\mathbf{r})/\psi_0(\mathbf{r})$ , from the data, using our model, yielding the phase data needed to compute the amplitude of each OAM mode and the average OAM normal to any domain. Note that since the reconstructed test wavefunction is given by  $\psi_1(\mathbf{r})/\psi_0(\mathbf{r})$ , we do not observe any coherence effects, as these are all contained within  $\psi_0(\mathbf{r})$ . Figure 5a, shows the real part of the reconstructed test wavefunction zoomed in on a single vortex. To calculate the amplitude of each OAM mode, we introduce a spatially averaged AFT

$$\bar{\psi}_t^{\ell} = \int_{\mathcal{D}} e^{i\ell\phi(x,y)} \psi_t(x,y) d^2\mathbf{x} \quad (24)$$

with  $\phi(x,y)$  defined by the argument between the x and y coordinate (i.e.,  $\phi = \text{Arg}(x + iy)$ ) and  $\mathcal{D}$  an arbitrary two dimensional domain, over which the average mode amplitude is to be determined. From the amplitudes calculated in Eq. (24) the expectation value of the OAM orthogonal to the domain surface can be determined

$$\langle L_z \rangle = \frac{\sum_{\ell} \ell |\bar{\psi}_t^{\ell}|^2}{\sum_{\ell} |\bar{\psi}_t^{\ell}|^2} \quad (25)$$

To closely approximate Eq. (15) a circular domain is chosen to calculate the amplitudes,  $\bar{\psi}_t^{\ell}$ , given by Eq. (24). To first order, it was shown that the  $\ell = \pm 1$  amplitudes increase linearly with  $\rho$  (Eq. (19)), hence a larger domain will see a larger maximal value of the OAM. We will, therefore, choose the maximal domain size on which the first order approximations of the test wavefunction are valid. The first order approximation can be used up to  $k_{\perp}\rho = 0.75$  with a maximal relative error of less than 0.1. In our setup, this corresponds to a domain size of 0.22 mm. Being much larger than the effective transverse coherence of the beam (roughly 5  $\mu\text{m}$ ) it follows that the OAM must be considered to be extrinsic. The domain on which the spatially averaged AFT is calculated is indicated in Fig. 5a. It can be scanned across the reconstructed test wavefunction,  $\psi_1(\mathbf{r})/\psi_0(\mathbf{r})$ , to calculate  $\langle L_z \rangle$  in each section of the image. This OAM expectation value is shown

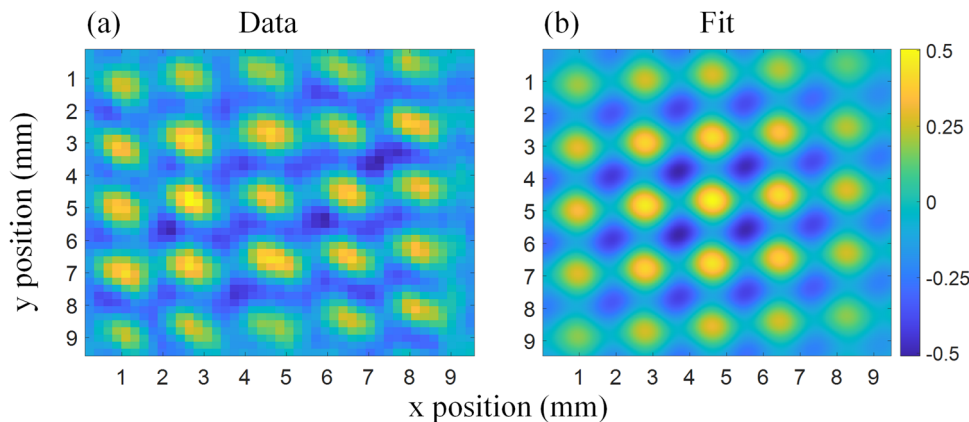


**Fig. 4 Measurement results and fit.** **a** The processed, normalized and filtered image of the neutron vortex lattice, recorded using the position sensitive detector seen in Fig. 1. The contrast, according to the fit **(b)** based on Eq. (23), is 0.53. The lattice period is 1.83 mm.

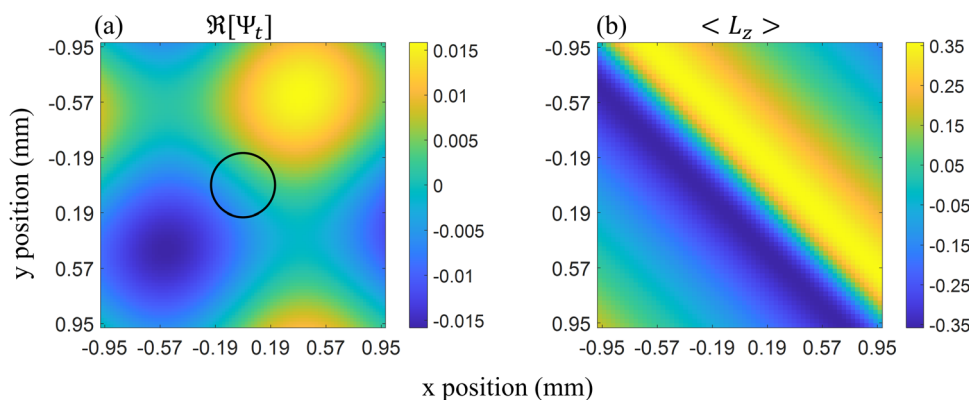


**Fig. 5 Reconstructed wavefunction and OAM expectation value.** **a** Image of the real part of the test wavefunction of a single vortex carrying extrinsic OAM. This test wavefunction is reconstructed using the fit parameters generated by the model shown in Fig. 4. A circle is drawn in the center of the image indicating the domain on which the spatially averaged AFTs are applied and the first order approximations used throughout the paper are valid. The axis around which the OAM is defined is centered on and normal to this circular domain. **b** The average extrinsic OAM ( $\langle L_z \rangle$ ) over the image is shown. This is calculated using the spatially averaged AFT (Eq. (24)) and Eq. (25).

in Fig. 5b. Note the diagonal (45 degree) “lines” of constant OAM in Fig. 5b, confirming the prediction made by Eq. (9).

## Discussion

We see that our method using only two prisms generates extrinsic vortices with a significant  $\ell = \pm 1$  component, such that the average beam OAM can reach up to  $|\langle L_z \rangle| \approx 0.35$ . While the vortex diameter is still much larger than the calculated coherence length and therefore cannot be applied to experiments requiring intrinsic OAM<sup>12,13,31</sup>, spatially modulated beams like the one generated in our setup can be applied to ultra small angle scattering. In numerous configurations it has been shown that one dimensional intensity modulation (such as Moire patterns) can be applied to ultra small angle scattering, for example, in neutron dark field imaging/Talbot-Lau interferometry<sup>33,34</sup> and spin echo modulated small angle neutron scattering<sup>35–37</sup>. With the exception of a recent development in Talbot-Lau interferometry<sup>38</sup> the latter methods can only measure the elastic scattering function  $S(q)$  in one dimension. Two dimensional intensity modulation, as generated by our setup, could be used to measure two dimensional elastic scattering functions, allowing analysis of anisotropic samples in a single measurement. Such a measurement would employ the same instrument as described in this paper. A sample could be placed between the interferometer and position sensitive detector. Small angle scattering from the sample would wash out the intensity

modulation leading to contrast reduction. This contrast reduction is proportional to the Fourier transform of  $S(q)$  analogous to spin-echo modulated small angle neutron scattering methods<sup>35,36</sup>. By Fourier transforming the modulated intensity pattern it is possible to separate the contrasts of the vertical and horizontal modulation. This allows the instrument to distinguish between vertical and horizontal scattering. Hence, the instrument could simultaneously measure  $S(q_x)$  and  $S(q_y)$ . This scheme could also be applied to the magnetic method for generating vortex lattices<sup>20</sup>. Both the latter method and our approach still lack the focusing prisms used for first order corrections to the divergence/coherence, which prevent dephasing and are available in the one dimensional method<sup>35–37</sup>. Though a recent analysis<sup>39</sup> has demonstrated how to implement first order divergence corrections in a setup analogous to the magnetic coherent averaging method<sup>20</sup> and the setup described in this paper. Focusing elements increase the modulation contrast and allow for larger beam sizes/divergences, thereby increasing the available intensity. These focusing prisms become a requirement when one looks towards generating intrinsic OAM using our method. Equation (8), shows that the refraction angle of the prisms or  $k_{\perp}$  must be on the same order of magnitude as the beam divergence or  $\zeta$ , such that the amplitude of the  $|\ell| = 1$  mode becomes significant. This may be achievable in the near future with recent developments in compound neutron optics<sup>40</sup> and micromachining<sup>41</sup>. In addition, steeper prisms made from more dense optical material can be employed in compound devices.

The additional space required by obligatory focusing prisms call for larger perfect crystal interferometers. Ongoing developments in neutron interferometry with split crystals may make this possible in the near future<sup>42</sup>. However a fundamental limit is reached as  $k_{\perp}$  approaches the beam divergence  $\zeta$  along the diffraction direction, as in this case, beams are only poorly diffracted by interferometer plates. For diffraction to efficiently occur the momentum shifted wavefunction  $\psi_0(\mathbf{k} - k_{\perp}\hat{j})$  must have significant overlap with the input wavefunction  $\psi_0(\mathbf{k})$ , which is defined by the angular acceptance of the interferometer.  $\hat{j}$  here refers to the direction normal to the crystal planes. As a result, we can estimate that  $k_{\perp}$  can be on the order of  $\zeta$ . Using Eq. (8) it can be shown that the OAM expectation value cannot exceed 0.1, due to the diffraction limit. Nonetheless, the diffraction limit can be avoided if one uses real space coherent averaging instead of momentum space coherent averaging as was done in this work. That is to say instead of using a composite wavefunction like Eq. (2) where the partial wavefunctions are shifted in momentum space with respect to one another, one could use a composite wavefunction where the partial wavefunctions are shifted in real space relative to each other.

$$\psi(\mathbf{r}) = \frac{1}{\sqrt{2}}[\psi_0(\mathbf{r} - \delta\hat{y}) + e^{i\Delta\alpha}\psi_0(\mathbf{r} - \delta\hat{x})] \quad (26)$$

Where real space separations,  $\delta$ , can be achieved using prism pairs. The Fourier transform of this wavefunction is

$$\psi(\mathbf{k}) = \frac{1}{\sqrt{2}}\psi_0(\mathbf{k})(e^{i\delta k_p \sin(\theta)} + e^{i\Delta\alpha}e^{i\delta k_p \cos(\theta)}) \quad (27)$$

with  $k_p$  denotes the transverse wavenumber, while  $\theta$  is the azimuthal angle in momentum space. One can see that this wavefunction is identical in form to the test wavefunction,  $\psi_t$  (see Eq. (4)) used throughout this manuscript. Since the OAM operator does not change form under a Fourier transform

$$\begin{aligned} -i\left[x\frac{\partial}{\partial y} - y\frac{\partial}{\partial x}\right] \mathcal{F} &\Leftrightarrow -i\left[k_x\frac{\partial}{\partial k_y} - k_y\frac{\partial}{\partial k_x}\right] \\ -i\frac{\partial}{\partial \phi} \mathcal{F} &\Leftrightarrow -i\frac{\partial}{\partial \theta} \end{aligned} \quad (28)$$

it follows that the OAM of Eq. (27) can be derived identically to that of Eq. (4), detailed in the Treatment of OAM section. Therefore the form of the OAM expectation value is identical to that which is described in Eq. (8). Contrary to what one may intuitively think the wavefunction in Eq. (27) does not obey  $\langle k_x \rangle = \langle k_y \rangle = 0$  it follows that, the OAM is therefore not invariant under translation (see Eq. (9)) and is therefore also not truly intrinsic. Though once again in some cases for translations within the coherence length, the OAM may be considered quasi-intrinsic. Moving forward in the pursuit of

neutron OAM real space coherent averaging methods should be applied since it is technically simpler to generate large real space displacements,  $\delta$  of the wavefunction, on the order of the neutron coherence  $\sigma$ , compared to generating large  $k_{\perp}$  on the order of the wavefunctions momentum spread  $\zeta$ . In summary, we argue that this work denotes an important step towards high yield OAM generating optical devices for thermal neutrons. Such devices will enable new scattering experiments which can access phase information of the scattering cross section<sup>12,13</sup>. Furthermore, the additional degree of freedom provided by the OAM quantum number would allow quadruple state entanglement in neutrons (energy, position, spin, and OAM), opening up new possibilities in the realm of quantum information and contextuality<sup>14,15</sup>. In addition, our theoretical analysis, which gives a condition for intrinsic particle OAM (adapted from optics<sup>29</sup>), provides a method for determining the probability amplitudes of each OAM mode and examines two special cases of coherent averaging in real and reciprocal space, may be useful in the design of future OAM generating neutron optical instrumentation. Especially the final analysis described in Eqs. (27)–(28) could greatly simplify intrinsic neutron OAM production by coherent averaging methods. Finally, we argued that the instrumentation in its current state could be applied to anisotropic ultra small angle neutron scattering, by observing the change in modulation contrast when a sample is placed between interferometer and detector.

## Methods

**Interferometry setup.** The four plate interferometer<sup>24–27</sup> is part of the S18 beamline situated at the high flux reactor of the Institute Laue Langevin (ILL) in Grenoble France<sup>23</sup>. Both the interferometer and the monochromator are cut from a perfect silicon crystal. Both utilize the 220 plane. For this experiment, a Bragg angle of  $30^\circ$  was used resulting in a wavelength of  $1.92 \text{ \AA}$  and a bandwidth of  $\Delta\lambda/\lambda \approx 0.02$ . Our  $5^\circ$  prisms were milled out of aluminium (type: EN AW-6060). We estimate a refraction angle of  $1.1 \cdot 10^{-7}$  rad or 0.022 arcseconds. The phase shifters consisted out of a polished 3 mm thick sapphire slab and a 3 mm thick silicon slab. A  $2 \times 2 \text{ mm}^2$  collimator was placed just downstream from the monochromator, roughly 3 m from the detector. The beam expanded to  $10 \times 10 \text{ mm}^2$  over this distance, indicating a maximal divergence of  $\sim 2$  mrad. This is used to calculate the vertical coherence. The rocking full width half maximum is around half a second of arc, which is used for calculating the horizontal coherence. A position sensitive detector, using a scintillator, a  $45^\circ$  mirror and a CCD camera was employed to record the Moire patterns. The resolution of the CCD camera was determined experimentally to be around  $22 \mu\text{m}$ , however, the scintillator limits the maximally achievable resolution to  $40 \mu\text{m}$ .

**Data processing.** The images shown in this paper were generated using two recorded datasets, the first with prisms inserted in the interferometer and the second without prisms. Each dataset consists of 14 recordings 30 min a piece. The raw images shown in Fig. 6 show the summed averages over all 14 images. To obtain the image shown in Fig. 4 both raw images (Fig. 6) are binned by a factor of  $10 \times 10$  squared pixels to increase statistics. Next, the binned “prisms-in” image is

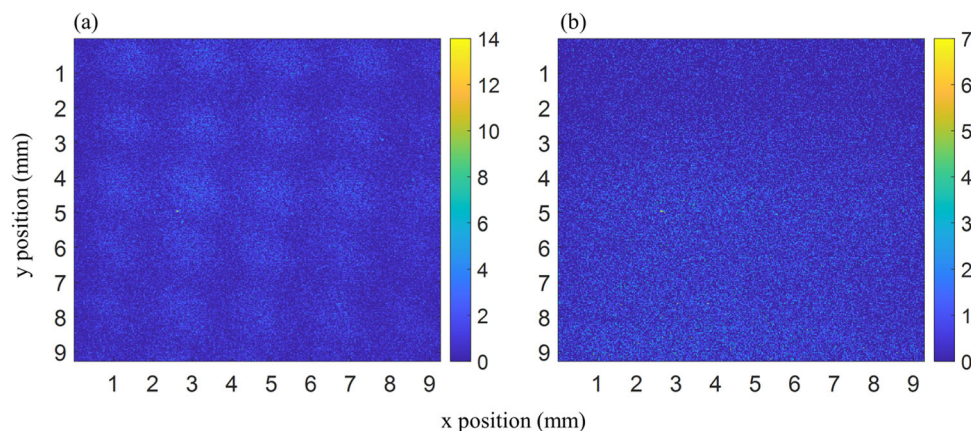


**Fig. 6 Raw datasets.** Sum over the raw datasets used to generate the figures shown in this paper. **a** Image with the prisms inserted. **b** Image of the intensity distribution without prisms in the interferometer.



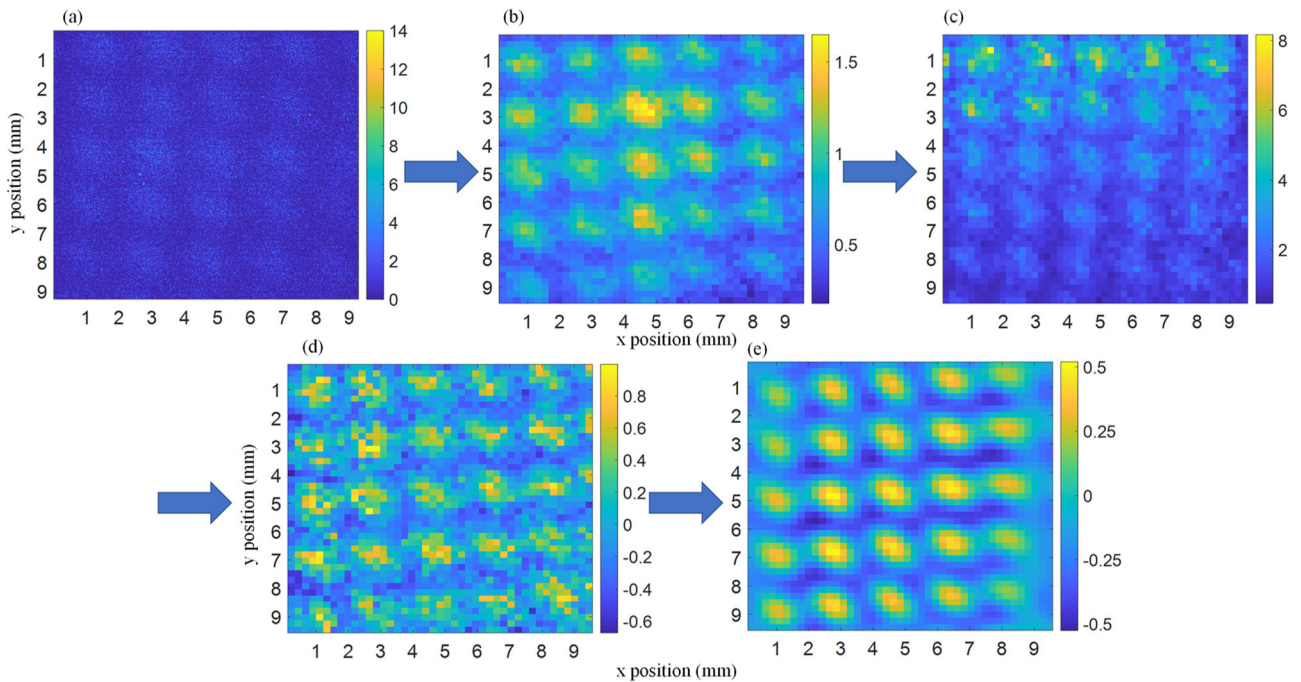


**Fig. 7 Step by step illustration of the image processing technique.** The raw image (a) is binned (b) by a factor of  $10 \times 10$  squared pixels. The first normalization is shown in (c), followed by the next normalization steps (d) by dividing by a quadratic polynomial and subsequently dividing by the mean intensity and subtracting one. Finally, the Fourier filter is applied resulting in the last image (e).

divided by the binned “prisms-out” image to remove artifacts induced by uneven illumination of the detector and spatial phase drifts inherent to the interferometer. After this initial normalization the resulting image still has a slight intensity drift over the vertical (y) direction. This is removed by fitting a quadratic polynomial to the average intensity along the vertical direction and dividing the image by this polynomial. After this step, the image is normalized by dividing it by the mean intensity and subtracting one  $I_{norm} = \frac{I}{\langle I \rangle} - 1$ . Finally a noise reduction scheme is applied to improve the overall signal quality. This is achieved by Fourier transforming the image, removing all content from the FT below a certain noise floor and transforming the modified FT back to real space. Figure 7 shows the image at each point of the data reduction.

**Fitting procedure.** The fit shown in Fig. 4 is based on Eq. (23), with a few modifications to take into account perturbations not considered in our simplified theory. By normalizing the data as described above, we forfeit the need for a constant offset in the fit function. In addition to account for the dephasing which reduces the contrast towards the edges of the image since the neutrons have to pass through more material, we multiply Eq. (23) by a Gaussian envelope. Finally, we note that the interference pattern in the images indicate that the prisms were not totally orthogonal, as a result, the fit function takes on the form

$$f = e^{-\frac{(\vec{x} - \vec{\mu})^2}{s^2}} [a_1 \cos(\vec{\eta}_1 \cdot \vec{x} + \alpha_1) + a_2 \cos(\vec{\eta}_2 \cdot \vec{x} + \alpha_2) + a_3 \cos((\vec{\eta}_1 - \vec{\eta}_2) \cdot \vec{x} + \alpha_1 - \alpha_2)] \quad (29)$$

Here initial guesses for  $\vec{\eta}_1$ ,  $\vec{\eta}_2$ ,  $\alpha_1$ ,  $\alpha_2$ ,  $a_1$ ,  $a_2$  and  $a_3$  are extracted from the Fourier transform of the processed data. An initial guess for  $\vec{\mu}$  is found by determining the expectation value of the squared processed data  $\langle \vec{x}^2 \rangle = \frac{\int dxdy \vec{x}^2 I^2}{\int dxdy I^2}$ . Finally the parameter  $s^2$  is guessed by calculating the variance of the squared processed data  $\frac{\int dxdy |\vec{x}^2|^2 I^2}{\int dxdy I^2} - \langle \vec{x}^2 \rangle^2$ .

## Data availability

The data that support the findings of this study are available online<sup>23</sup>.

Received: 20 June 2022; Accepted: 25 July 2023;

Published online: 09 August 2023

## References

- Allen, L., Beijersbergen, M., Spreeuw, R. & Woerdman, J. Orbital angular momentum of light and the transformation of Laguerre-Gaussian laser modes. *Phys. Rev. A* **45**, 8185 (1992).
- van Enk, S. J. & Nienhuis, G. Spin and orbital angular momentum of photons. *EPL* **25**, 497 (1994).
- Molina-Terriza, G., Torres, J. & Torner, L. Twisted photons. *Nat. Phys.* **3**, 305–310 (2007).
- Gibson, G. et al. Free-space information transfer using light beams carrying orbital angular momentum. *Opt. Express* **12**, 5448–5456 (2004).
- Harwit, M. Photon orbital angular momentum in astrophysics. *Astrophys. J.* **597**, 1266 (2003).
- Padgett, M. J. Orbital angular momentum 25 years on [invited]. *Opt. Express* **25**, 11265–11274 (2017).
- Uchida, M. & Tonomura, A. Generation of electron beams carrying orbital angular momentum. *Nature* **464**, 737 (2010).
- McMorran, B. J. et al. Electron vortex beams with high quanta of orbital angular momentum. *Science* **331**, 192–195 (2011).
- Luski, A. et al. Vortex beams of atoms and molecules. *Science* **373**, 1105 (2021).
- Clark, C. W. et al. Controlling neutron orbital angular momentum. *Nature* **525**, 504–506 (2015).
- Sarenac, D. et al. Experimental realization of neutron helical waves. *Sci. Adv.* **8**, eadd2002 (2022).
- Afanasev, A., Karlovets, D. & Serbo, V. Schwinger scattering of twisted neutrons by nuclei. *Phys. Rev. C* **100**, 051601 (2019).
- Afanasev, A., Karlovets, D. & Serbo, V. Elastic scattering of twisted neutrons by nuclei. *Phys. Rev. C* **103**, 054612 (2021).
- Hasegawa, Y. et al. Engineering of triply entangled states in a single-neutron system. *Phys. Rev. A* **81**, 032121 (2010).
- Shen, J. et al. Unveiling contextual realities by microscopically entangling a neutron. *Nat. Commun.* **11**, 930 (2020).
- Nsofini, J. et al. Spin-orbit states of neutron wave packets. *Phys. Rev. A* **94**, 013605 (2016).
- Sarenac, D. et al. Methods for preparation and detection of neutron spin-orbit states. *New J. Phys.* **20**, 103012 (2018).
- Ishihara, J. et al. Imprinting spatial helicity structure of vector vortex beam on spin texture in semiconductors. *Phys. Rev. Lett.* **130**, 126701 (2023).
- Cappelletti, R., Jach, T. & Vinson, J. Intrinsic orbital angular momentum states of neutrons. *Phys. Rev. Lett.* **120**, 090402 (2018).
- Sarenac, D. et al. Generation and detection of spin-orbit coupled neutron beams. *PNAS* **116**, 20328–20332 (2019).



21. Geerits, N. & Sponar, S. Twisting neutral particles with electric fields. *Phys. Rev. A* **103**, 022205 (2021).
22. Sarenac, D. et al. Holography with a neutron interferometer. *Opt. Express* **24**, 22528–22535 (2016).
23. Geerits, N., Berger, A. & Lemmel, H. Generation of neutron spin-orbit states. <https://doi.org/10.5291/ILL-DATA.CRG-2883> (2021).
24. Heinrich, M., Petrascheck, D. & Rauch, H. Test of a four plate neutron interferometer. *Zeitschrift für Physik B Condensed Matter* **72**, 357–363 (1988).
25. Hasegawa, Y., Zawisky, M., Rauch, H. & Ioffe, A. I. Geometric phase in coupled neutron interference loops. *Phys. Rev. A* **53**, 2486–2492 (1996).
26. Filipp, S., Hasegawa, Y., Loidl, R. & Rauch, H. Noncyclic geometric phase due to spatial evolution in a neutron interferometer. *Phys. Rev. A* **72**, 021602 (2005).
27. Geppert-Kleinrath, H. et al. Multifold paths of neutrons in the three-beam interferometer detected by a tiny energy kick. *Phys. Rev. A* **97**, 052111 (2018).
28. Berry, M. V. *Proc. Paraxial beams of spinning light SPIE* **3487**, 6–11 (1998).
29. O’Neil, A. T., MacVicar, I., Allen, L. & Padgett, M. J. Intrinsic and extrinsic nature of the orbital angular momentum of a light beam. *Phys. Rev. Lett.* **88**, 053601 (2002).
30. Abramowitz, M. & Stegun, I. *Handbook of Mathematical Functions with Formulas, Graphs, and Mathematical Tables* (Cambridge University Press, 1964).
31. Jach, T. & Vinson, J. Method for the definitive detection of orbital angular momentum states in neutrons by spin-polarized  $^3\text{He}$ . *Phys. Rev. C* **105**, L061601 (2022).
32. Sarenac, D. et al. Generation of a lattice of spin-orbit beams via coherent averaging. *PRL* **121**, 183602 (2018).
33. Strobl, M. et al. Neutron dark-field tomography. *Phys. Rev. Lett.* **101**, 123902 (2008).
34. Strobl, M. et al. Wavelength-dispersive dark-field contrast: micrometre structure resolution in neutron imaging with gratings. *J. Appl. Cryst.* **49**, 569–573 (2016).
35. Bouwman, W. G., Duif, C. P. & Gahler, R. Spatial modulation of a neutron beam by Larmor precession. *Phys. B* **404**, 2585–2589 (2009).
36. Bouwman, W. G., Duif, C. P., Plomp, J., Wiedenmann, A. & Gahler, R. Combined sans-sesans, from 1 nm to 0.1 mm in one instrument. *Phys. B* **406**, 2357–2360 (2011).
37. Li, F. et al. Spin echo modulated small-angle neutron scattering using superconducting magnetic Wollaston prisms. *J. Appl. Crystallogr.* **49**, 55–63 (2016).
38. Valsecchi, J. et al. Characterization of oriented microstructures through anisotropic small-angle scattering by 2d neutron dark-field imaging. *Commun. Phys.* **3**, 42 (2020).
39. Thien, Q. L., McKay, S., Pynn, R. & Ortiz, G. Spin-textured neutron beams with orbital angular momentum. *Phys. Rev. B* **107**, 134403 (2023).
40. Adachi, T. et al. Development of neutron compound refractive optics: a progress report. *Appl. Phys. A* **74**, S180–S182 (2002).
41. Kapahi, C. et al. Next-generation high transmission neutron optical devices utilizing micro-machined structures. *arXiv:2112.13176* (2021).
42. Lemmel, H. et al. Neutron interference from a split-crystal interferometer. *J. Appl. Cryst.* **55**, 870–875 (2022).

## Acknowledgements

This work was funded by the Austrian Science Fund (FWF), Project No. P34239.

## Author contributions

N.G., H.L., and S.S. conceived the experiment; N.G., H.L., and A.B. carried out the experiment; N.G. analyzed the data; N.G. wrote the paper with contributions from all authors.

## Competing interests

The authors declare no competing interests.

## Additional information

**Supplementary information** The online version contains supplementary material available at <https://doi.org/10.1038/s42005-023-01318-6>.

**Correspondence** and requests for materials should be addressed to Niels Geerits or Stephan Sponar.

**Peer review information** *Communications Physics* thanks Fred Wietfeldt, Dmitry Karlovets and the other anonymous, reviewers for their contribution to the peer review of this work.

**Reprints and permission information** is available at <http://www.nature.com/reprints>

**Publisher’s note** Springer Nature remains neutral with regard to jurisdictional claims in published maps and institutional affiliations.



**Open Access** This article is licensed under a Creative Commons Attribution 4.0 International License, which permits use, sharing, adaptation, distribution and reproduction in any medium or format, as long as you give appropriate credit to the original author(s) and the source, provide a link to the Creative Commons license, and indicate if changes were made. The images or other third party material in this article are included in the article’s Creative Commons license, unless indicated otherwise in a credit line to the material. If material is not included in the article’s Creative Commons license and your intended use is not permitted by statutory regulation or exceeds the permitted use, you will need to obtain permission directly from the copyright holder. To view a copy of this license, visit <http://creativecommons.org/licenses/by/4.0/>.

© The Author(s) 2023